
Article:
Geers, AJ, Morales, HG, Larrabide, I et al. (3 more authors) (2017) Wall shear stress at the initiation site of cerebral aneurysms. Biomechanics and Modeling in Mechanobiology, 16 (1). pp. 97-115. ISSN 1617-7959

https://doi.org/10.1007/s10237-016-0804-3

Biomechanics and Modeling in Mechanobiology manuscript No.
(will be inserted by the editor)

Wall shear stress at the initiation site of cerebral aneurysms

A.J. Geers · H.G. Morales · I. Larrabide · C. Butakoff · P. Bijlenga · A.F. Frangi

Received: date / Accepted: date

Abstract Hemodynamics are believed to play an important role in the initiation of cerebral aneurysms. In particular, studies have focused on wall shear stress (WSS), which is a key regulator of vascular biology and pathology. In line with the observation that aneurysms predominantly occur at regions of high WSS, such as bifurcation apices or outer walls of vascular bends, correlations have been found between the aneurysm initiation site and high WSS. The aim of our study was to analyze the WSS field at an aneurysm initiation site that was neither a bifurcation apex nor the outer wall of a vascular bend. Ten cases with aneurysms on the A1 segment of the anterior cerebral artery (ACA) were analyzed and compared with ten controls. Aneurysms were virtually removed from the vascular models of the cases to mimic the pre-aneurysm geometry. Computational fluid dynamics (CFD) simulations were created to assess the magnitude, gradient, multidirectionality, and pulsatility of the WSS. To aid the inter-subject comparison of hemodynamic variables, we mapped the branch surfaces onto a two-dimensional parametric space. This approach made it

Preliminary findings from this study were presented at the International Symposium on Biomechanics in Vascular Biology and Cardiovascular Disease, Montreal, QC, Canada, 28–29 April 2014 and at the European Solid Mechanics Conference, Madrid, Spain, 6–10 July 2015.

A.J. Geers
CISTIB, Universitat Pompeu Fabra, Barcelona, Spain
E-mail: ajgeers@gmail.com

H.G. Morales
Medisys – Philips Research Paris, Paris, France

I. Larrabide
PLADEMA-CONICET, UNICEN, Tandil, Argentina

C. Butakoff
PhySense, Universitat Pompeu Fabra, Barcelona, Spain

P. Bijlenga
Hôpitaux Universitaire de Genève et Faculté de médecine de Genève, Geneva, Switzerland

A.F. Frangi
CISTIB, University of Sheffield, Sheffield, UK

possible to view the whole branch at once for qualitative evaluation. It also allowed us to define a patch for quantitative analysis, which was consistent among subjects and encapsulated all aneurysm initiation sites. To test the reproducibility of our results, CFD simulations were repeated with a second independent observer virtually removing the aneurysms and with a 20 % higher flow rate at the inlet. We found that branches harboring aneurysms were characterized by high WSS and high WSS gradients. Among all assessed variables, the aneurysm initiation site most consistently coincided with peaks of temporal variation in the WSS magnitude.

Keywords aneurysm initiation · cerebral aneurysms · computational fluid dynamics · hemodynamics · image-based modeling · flow pulsatility · wall shear stress

1 Introduction

Cerebral aneurysms are localized, pathological dilatations of cerebral arteries. Their rupture causes subarachnoid hemorrhage and is associated with high rates of morbidity and mortality (Hop et al, 1997). Better understanding of the mechanisms underlying aneurysm initiation is crucial for the development of new preventive and therapeutic strategies (Jamous et al, 2005).

While systemic risk factors such as hypertension and connective tissue disorders may weaken the cerebral arteries' ability to maintain homeostasis, hemodynamic stress appear to be a necessary trigger for the pathological remodeling leading to aneurysm formation (Brown et al, 1990; Stehbens, 1989; Nixon et al, 2010; Penn et al, 2011; Dolan et al, 2013; Sadasivan et al, 2013; Meng et al, 2014; Frösen, 2014; Turjman et al, 2014). In vivo measurements of these stresses are limited by the low spatial and temporal resolution of current imaging techniques (Markl et al, 2012) and the rarity of imaging a patient prior to aneurysm formation. Instead, computational fluid dynamics (CFD) techniques have been employed to simulate the hemodynamics in vascular geometries with the aneurysm virtually removed to approximate the pre-aneurysm condition (Mantha et al, 2006; Baek et al, 2009; Ford et al, 2009; Shimogonya et al, 2009; Singh et al, 2010; Castro et al, 2011; Chen et al, 2013; Kono and Terada, 2013; Lauric et al, 2014) and in vascular geometries derived from rare pre-aneurysm images (Doenitz et al, 2010; Kulcsar et al, 2011; Kono and Terada, 2013; Kono et al, 2014). CFD simulations have also been used to complement histological analyses of aneurysm formation in animal models (Meng et al, 2007; Metaxa et al, 2010).

Hemodynamic studies have strongly focused on wall shear stress (WSS), which is a key regulator of vascular biology and pathology (Dolan et al, 2013). In line with the observation that aneurysms predominantly occur at high WSS regions such as bifurcation apices or outer walls of vascular bends (Kondo et al, 1997; Alnaes et al, 2007; Piccinelli et al, 2011; Alfano et al, 2013), many studies have found correlations between the aneurysm initiation site and high WSS (Castro et al, 2011; Singh et al, 2010; Chen et al, 2013), especially in combination with high positive WSS gradients (WSSG) (Meng et al, 2007; Metaxa et al, 2010; Kulcsar et al, 2011; Kono and Terada, 2013; Kono et al, 2014). Other studies have found correlations with low WSS (Mantha et al, 2006; Doenitz et al, 2010), WSS patterns involving both high and low

WSS (Baek et al, 2009; Lauric et al, 2014), or indices describing the oscillatory nature of the WSS and WSSG (Mantha et al, 2006; Ford et al, 2009; Shimogonya et al, 2009; Chen et al, 2013). These apparent inconsistencies among CFD-based studies can be attributed to the small datasets, variety of aneurysm locations, and subjectivity of data analyses, as pointed out by Chen et al. (Chen et al, 2013), but also to missing patient-specific information about boundary conditions and properties of the arterial wall.

The aim of our study was to analyze the WSS field at the aneurysm initiation site. All included aneurysms were from a single location, which was neither a bifurcation apex nor the outer wall of a vascular bend. Vascular geometries with the aneurysm removed were matched to controls that never formed an aneurysm at that particular location but elsewhere. To standardize the data analysis and simplify the comparison of cases, branches of interest were mapped onto the same parametric space. Tests were performed to measure the reproducibility of the computed WSS field with respect to the observer virtually removing the aneurysm and the flow rate imposed at the inlet.

2 Methods

2.1 Case selection

Twenty patients, ten cases and ten controls, were drawn from a large multicenter database created within the EU-funded project @neurIST (Villa-Uriol et al, 2011). The data collection protocol was approved by individual local ethics committees, and written consent was obtained from patients or, where appropriate, next of kin. The cases were all the patients in the database with an aneurysm on the A1 segment of the anterior cerebral artery (ACA). They were selected because of their remarkable consistency in aneurysm location: all aneurysms were just distal to the internal carotid artery (ICA) bifurcation with nine cases directed posteriorly (cases 1 to 9) and one case directed anteriorly (case 10). Moreover, the location was neither a bifurcation apex nor the outer wall of a vascular bend, which – attributed to being high WSS regions – are the most common aneurysm locations (Kondo et al, 1997; Alnaes et al, 2007; Piccinelli et al, 2011; Alfano et al, 2013). The controls were patients with an aneurysm at the middle cerebral artery (MCA) bifurcation, hence predisposed to having aneurysms, that did not form an aneurysm at the studied location on the A1 segment of the ACA. They were selected to match cases by patient age (within 2 years) and aneurysm hemisphere (left or right). No other information was considered during the selection process.

2.2 Vascular modeling

Patient-specific vascular models, represented by triangular surface meshes, were constructed by segmenting three-dimensional rotational angiography (3DRA) images using a geodesic active regions approach (Bogunović et al, 2011). The ophthalmic

artery, anterior choroidal artery, and posterior communicating artery branching off the ICA were preserved if successfully segmented. Touching vessels were removed. Models were smoothed using a geometry-preserving smoothing algorithm (Nealen et al, 2006). To ensure consistency in the extent of the vascular models, inlet and outlet branches were clipped at the same location for all cases and controls. Inlet branches were clipped at a manually selected location at the start of the cavernous segment of the ICA and then extruded 10 mm to allow for flow to develop. Outlet branches were automatically clipped 10 mm from their proximal bifurcation; those shorter than 10 mm were first extruded. The ACA had to be extruded only for control 6. Figure 1 shows the vascular models of all cases and controls.

Aneurysms were virtually removed from the vascular models of the cases to mimic the pre-aneurysm geometry (Figure 1). Triangle removal and hole filling operations were iteratively applied to reconstruct the ACA without aneurysm. Subsequently, the vascular model was smoothed and inlet and outlet branches were clipped as described in the previous paragraph. To assess the reproducibility of the computed WSS field with respect to this manual procedure, two observers independently removed the aneurysm for all cases.

The automatic selection of outlet locations made use of centerlines and bifurcation origins generated with the Vascular Modeling Toolkit (VMTK) (Antiga et al, 2008; Piccinelli et al, 2009). Manual mesh editing operations were performed in @neuFuse (B3C, Bologna, Italy) (Villa-Uriol et al, 2011), a software application developed within @neurIST.

2.3 Blood flow modeling

Unstructured volumetric meshes were created with ICEM CFD 13.0 (ANSYS, Canonsburg, PA, USA) using an octree approach. Meshes were composed of tetrahedral elements with a side length of 0.2 mm and three prism layers with a total height of 0.07 mm and a side length of 0.1 mm. The total number of elements ranged from 2.3 to 6.7 million, the density from 3124 to 4076 elements per mm^3, depending on the surface-area-to-volume ratio of the computational domain. This mesh resolution was chosen following previously performed mesh dependency tests (Geers et al, 2014).

CFD simulations were created with CFX 13.0 (ANSYS), which is a commercial vertex-centered finite volume solver. We used a second-order advection scheme and a second-order backward Euler transient scheme. Solutions converged until the normalized residual of the WSS everywhere in the computational domain was $< 5 \times 10^{-4}$.

Blood was modeled as an incompressible Newtonian fluid with density $\rho = 1060\,kg/m^3$ and viscosity $\mu = 4\,mPa\,s$. Although blood is a non-Newtonian fluid, assuming constant viscosity is appropriate for our problem (Morales et al, 2013). Vessel walls were assumed rigid with a no-slip boundary condition. A parabolic velocity profile was imposed at the inlet.

Since patient-specific flow information was unavailable, we estimated the flow rate waveform at the inlet and imposed zero-pressure boundary conditions at all outlets. The shape of the flow rate waveform was obtained from Ford et al. who averaged the waveform shapes of 17 young, normal volunteers (Ford et al, 2005). The

time-averaged flow rate, Q, was obtained using the relationship from Cebral et al.: $Q = 48.21\,A^{1.84}\,T^{-1}$ where Q is in ml/s, A is the inlet's cross-sectional area in cm^2, and T is the period of the cardiac cycle in s. This relationship was obtained by fitting a power-law function through measurements of Q and A of the ICAs and vertebral arteries of 11 normal volunteers (Cebral et al, 2008). Reynolds numbers at the inlets ranged from 62 to 441 with an average of 152. To assess the reproducibility of the computed WSS field with respect to boundary conditions, we repeated the simulations for all cases and controls with a 20 % higher flow rate at the inlet.

The cardiac cycle was discretized in 200 uniformly distributed time steps and, to reduce the effect of initial transients, the second of two simulated cardiac cycles was analyzed. These settings were chosen following previously performed time step and cycle dependency tests (Geers et al, 2014).

A total of 50 CFD simulations were created: 10 cases and 10 controls under 'normal' inflow conditions, 10 cases and 10 controls under 'high' inflow conditions, and 10 cases under 'normal' inflow conditions with the aneurysm removed by the second observer.

2.4 Hemodynamic variables

As mentioned in the Introduction (Section 1), different aspects of the WSS field are deemed relevant to the initiation of aneurysms. Specifically, we assessed the magnitude, gradient, multidirectionality, and pulsatility of the WSS, according to the definitions below.

Given WSS vector $\tau_w = \tau_w(x,t)$ at surface point x and time t, the time-averaged WSS magnitude (TAWSS) is defined as

$$\mathrm{TAWSS} = \frac{1}{T}\int_0^T |\tau_w|\,\mathrm{d}t \tag{1}$$

where T is the period of the cardiac cycle.

For use in the definition of other WSS-related variables, we defined unit vectors in the direction of and perpendicular to the time-averaged WSS vector, respectively $\hat{p}$ and $\hat{q}$, as

$$\hat{p} = \frac{\int_0^T \tau_w\,\mathrm{d}t}{\left|\int_0^T \tau_w\,\mathrm{d}t\right|}, \qquad \hat{q} = \hat{p}\times\hat{n} \tag{2}$$

where $\hat{n}$ is the surface normal.

For the gradient of TAWSS (TAWSSG), we used the definition proposed by Meng and colleagues (Tremmel et al, 2010; Dolan et al, 2013), which differentiates between positive and negative gradients with respect to $\hat{p}$, namely,

$$\mathrm{TAWSSG} = \nabla_S(\mathrm{TAWSS})\cdot\hat{p} \tag{3}$$

where ∇_S is the gradient on the vessel wall surface.

Throughout the cardiac cycle, the WSS vector may change direction and not remain parallel to $\hat{p}$. The changing WSS direction is associated with the concept of

'disturbed' flow. To quantify the multidirectionality of disturbed flow, we used the transverse WSS (transWSS), which was recently proposed by Peiffer et al. in the context of atherosclerosis (Peiffer et al, 2013a). The transWSS is defined as the time-averaged absolute value of the q-component of the WSS vector, that is,

$$\text{transWSS} = \frac{1}{T}\int_0^T |\tau_w \cdot \hat{q}|\, \mathrm{d}t \tag{4}$$

We quantified the temporal variation in the WSS magnitude during the cardiac cycle by calculating the WSS pulsatility index (WSSPI) (Gosling and King, 1974), given by

$$\text{WSSPI} = \frac{\max\limits_{t\in[0,T]} \tau_w - \min\limits_{t\in[0,T]} \tau_w}{\text{TAWSS}} \tag{5}$$

As the WSS *magnitude* may vary substantially between CFD simulations using either patient-specific or estimated boundary conditions, caution in interpretation must be exercised (Karmonik et al, 2010; Marzo et al, 2011; Jansen et al, 2014; McGah et al, 2014). We chose to focus on the WSS *distribution* by normalizing TAWSS by the space-averaged TAWSS on the branch ($\overline{\text{TAWSS}}_\text{B}$). For aneurysms, normalized WSS distributions have been shown to remain relatively unchanged across a range of physiological boundary conditions (Marzo et al, 2011). TAWSSG and transWSS were similarly normalized by $\overline{\text{TAWSS}}_\text{B}$. Unless stated otherwise, we will report on normalized values.

2.5 Geometric variables

Vascular geometry has a major impact on hemodynamics (Geers et al, 2011) and indeed bifurcations harboring aneurysms tend to more strongly deviate from the optimality principle (Baharoglu et al, 2014). To complement the hemodynamic analysis in our study, we characterized the vascular geometry using the framework presented by Piccinelli et al. (Piccinelli et al, 2009), which is available as part of VMTK. We will briefly outline the procedure. Some of the processing steps are illustrated in Figure 2. For more details, refer to (Piccinelli et al, 2009).

Two centerlines were created: one from the inlet to the MCA outlet and another from the inlet to the ACA outlet. At the ICA bifurcation, the two centerlines diverged into their respective branches and the corresponding bifurcation origin and plane were identified. The normal to the bifurcation plane was set to point posteriorly. Centerlines were split into branches corresponding to the ICA, MCA, and ACA.

For each branch, a representative cross sectional area A was defined as the mean surface area of two cross sections. These two sections were created one and two maximally inscribed sphere radii away from the bifurcation. The bifurcation's area ratio (Ingebrigtsen et al, 2004) was given by

$$\text{area ratio} = \frac{A_\text{ACA} + A_\text{MCA}}{A_\text{ICA}} \tag{6}$$

Vectors pointing in the direction of the branches were created and then projected onto the bifurcation plane. The in-plane ICA-ACA and ICA-MCA angles were calculated.

To quantify the tortuosity of the ACA, we used the definition

$$\text{tortuosity} = \frac{L}{D} - 1 \tag{7}$$

where L is the length along the centerline and D is the Euclidean distance between its endpoints.

2.6 Branch extraction and parametrization

To aid the inter-subject comparison of hemodynamic variables on the surface of the ACA, we used the approach proposed by Antiga et al. (Antiga and Steinman, 2004), which is also available as part of VMTK. Briefly, the vessel wall surface was split into branches corresponding to the previously split centerlines (Figure 2). As branches are topologically equivalent to cylinders, the ACA could be mapped onto a two-dimensional (2D) parametric space with a longitudinal coordinate, u, and a periodic circumferential coordinate, v. Coordinate u ranged from 0 to 10 mm, increasing in the direction of the flow. Coordinate v ranged from $-\pi$ to π rad. The position of $v = 0$ was determined by the bifurcation normal parallel transported along the centerline and $v > 0$ was set to correspond to the superior side of the ACA.

2.7 Data visualization

Contour plots were created to visualize the distribution of hemodynamic variables on the surface of the ACA. Using the 2D parametrization, the branch surface was flattened onto a rectangle such that u and v corresponded to the vertical and horizontal axes of the plots, respectively (Figure 2). This approach made it possible to view the whole branch at once and more easily compare between subjects. Because the circumferential coordinate is periodic, we slightly extended the plot to range from -4 to 4 rad, thus maintaining a visual continuity of the variable distributions. To indicate the location of the aneurysm neck, we calculated the distance from the surface with aneurysm to the surface without aneurysm and plotted a contour line at 0.1 mm. The region enclosed by the aneurysm neck will be referred to as ‘aneurysm initiation site’.

2.8 Statistical analysis

In this study, we assessed the reproducibility of the computed WSS field with respect to the observer virtually removing the aneurysm and to the flow rate imposed at the inlet. Differences between solutions were quantified by calculating the root-mean-square deviation (RMSD) between TAWSS fields, after linearly interpolating them onto a uniformly remeshed branch surface with a nominal node spacing of 0.05 mm. Solutions of observer 2 were projected onto the remeshed branch surface of observer

1. Since normalized TAWSS fields were considered, for which $\overline{\mathrm{TAWSS}}_{\mathrm{B}} = 1$, the RMSD was equal to the coefficient of variation of the RMSD (CVRMSD). CVRMSD will be expressed as a percentage.

Space-averaged values of variables were calculated for quantitative analysis. Besides analyzing the whole branch, we defined a 'patch' that encapsulated all aneurysm initiation sites. This patch was bound by $u \in [0,5]$ and $v \in [-\pi/2\,,\,\pi/2]$, see Figure 2. For case 10, with the aneurysm directed anteriorly, and its matching control, the patch was defined at the opposite side of the branch, bound by $u \in [0,5]$ and $v \in [-\pi,\,-\pi/2\,) \cup (\,\pi/2\,,\pi]$. Variables were averaged over the branch, patch, and non-patch (branch minus patch).

To test the significance of the differences between regions and between cases and controls, we used the Wilcoxon signed-rank test for paired samples and the Wilcoxon rank-sum test for unpaired samples. Differences were considered statistically significant for $p < 0.05$. The following samples were compared: I. patch vs. non-patch for the cases (paired), II. patch vs. non-patch for the controls (paired), III. patches of the cases vs. patches of the controls (unpaired), and IV. branches of the cases vs. branches of the controls (unpaired).

The Wilcoxon rank-sum test was also used to compare geometric variables between cases and controls. Again, differences were considered statistically significant for $p < 0.05$.

3 Results

3.1 Geometry

As mentioned in Section 2.1, cases in this study were remarkably consistent in location, which is also confirmed by the location of the aneurysm initiation site in Figure 3. For cases 1 to 9, the circumferential coordinate of the center of the initiation site was on average 2° (range: −24 to 13°). For case 10, it was 119°. In other words, most aneurysms were approximately aligned with the transported bifurcation normal.

Table 1 reports on the statistical analysis of geometric variables. Bifurcation angles were very similar among cases and controls. Cross sectional areas of branches tended to be larger for cases, but only for the MCA branch these differences were statistically significant. Area ratios were not significantly different. The tortuosity of ACAs showed a non-significant trend of being larger for cases than for controls.

3.2 Hemodynamics

Figure 3 shows for all cases and controls the non-normalized TAWSS on the ACA. There were large variations in space-averaged TAWSS with values ranging from 1.0 to 11.2 Pa (mean: 3.5 Pa; standard deviation: 2.2 Pa). Figure 4 shows the normalized TAWSS, highlighting the distribution rather than the magnitude. Overall, cases appeared to have a larger spatial variation in TAWSS, covering a wider range of TAWSS

values. Close to the apex of the bifurcation and on the superior side of the ACA (Figure 2), TAWSS was relatively high for cases. However, some controls showed similar patterns, e.g. control 3 and control 5, whereas some cases, e.g. case 6, did not. Aneurysm initiation sites partly overlapped with regions of high TAWSS, yet tended to be near the edge of them. Statistical analysis revealed no significant differences between the patch and the rest of the branch (non-patch) for controls, but did show significant differences between those regions for cases (Table 2). Also, patches of cases experienced significantly higher TAWSS than those of controls. By definition, normalization removed differences in TAWSS between branches.

Figure 5 shows the distribution of TAWSSG. Cases' larger spatial variation in TAWSS was reflected by higher positive and negative gradients. Correspondingly, the absolute value of TAWSSG was significantly higher, both for the whole branch and for the patch (Table 2). Although magnitudes varied, distributions were found to be similar for cases and controls: patches experienced significantly higher absolute TAWSSG than the rest of the branch. However, there was no clear correlation between either positive or negative gradients and the aneurysm initiation site.

Figure 6 shows the distribution of transWSS. Concentrated regions of high transWSS were observed. WSS vectors changed direction more strongly closer to the ICA bifurcation, which is also reflected by patches having significantly higher transWSS than non-patches (Table 2). On average, transWSS was higher for cases than controls, but only for the whole branch these differences were significant. No clear correlations were found between regions of high transWSS and the aneurysm initiation site.

Animations of the WSS field during the cardiac cycle showed that, although the WSS magnitude obviously changed over time, the distribution remained relatively unchanged. Please refer to (Geers et al, 2015a) to view the animations online. This means that at each point on the branch the WSS magnitude over time resembled the shape of a typical flow rate waveform, which motivated our choice for describing the temporal variation with the pulsatility index. Figure 7 shows the distribution of WSSPI. Similar patterns could be observed among cases and controls. Near the bifurcation, regions of relatively high WSSPI were located on the posterior and anterior side of the ACA and regions of relatively low WSSPI were located on the superior and inferior side (See Figure 2C for a location guide). Further downstream, WSSPI was also relatively low. As a result, we found significant differences between patches and non-patches (Table 2). The main difference between cases and controls was that WSSPI was on average higher for cases, a significant difference for branches but not for patches. Judging from the contour plots, however, we did observe a clear correlation between WSSPI peaks and the aneurysm initiation site. Additional statistical analysis confirmed this observation by revealing that WSSPI was significantly higher for just the initiation site than for the whole patch (1.61 vs. 1.52, $p = 0.007$), which was not true for any of the other variables. In other words, among the assessed hemodynamic variables, WSSPI most consistently correlated with the aneurysm initiation site.

No pattern was found explaining the deviating aneurysm orientation of case 10. Removing the case and its matching control from analysis did not alter the observed trends.

3.3 Reproducibility analysis

Figure 8 shows the differences in TAWSS distribution between the observers manually removing the aneurysm and between 'normal' and 'high' flow rates at the inlet. For each comparison, we chose three representative cases or controls, corresponding to minimum, closest-to-mean and maximum CVRMSD. Good reproducibility was found between observers and, although increasing the flow rate by 20 % increased the average TAWSS magnitude by 28 %, the TAWSS distribution remained relatively unchanged. CVRMSD between observers was 6.17 ± 0.07 % (mean $\pm$ standard error), range: 3.57 to 8.05 %. CVRMSD between flow rates was 3.96 ± 0.04 %, range: 2.73 to 5.21 %.

4 Discussion

4.1 Main contributions and findings

In summary, the main contributions of this study are: 1. the dataset was drawn from a multicenter database and was composed of cases with aneurysms at a single location, which was not in a known region of high WSS, and a matching set of controls, 2. objective comparison of variable distributions was made possible by automatic extraction and parametrization of the branch, 3. to our knowledge, this is the first study to evaluate the transWSS and WSSPI in the context of aneurysm initiation; and 4. tests were performed to assess the reproducibility of the computed WSS field with respect to the observer virtually removing the aneurysm and the flow rate imposed at the inlet.

The main findings of this study are: 1. aneurysms form on branches with large spatial variations in TAWSS, as also reflected by the presence of high TAWSSG gradients; 2. aneurysms form on branches with large temporal variations in WSS direction (i.e. transWSS); 3. aneurysms form at regions of high TAWSS; and 4. aneurysms form at focal regions with large temporal variations in WSS magnitude (i.e. WSSPI).

4.2 Aneurysm location

The majority of aneurysms are found at the apex of bifurcations or the outer wall of vascular bends, which has long established the importance of hemodynamic stress in the initiation of cerebral aneurysms (Kayembe et al, 1984; Stehbens, 1989; Gonzalez et al, 1992; Kondo et al, 1997; Foutrakis et al, 1999). At the bifurcation apex, blood impinges the wall and rapidly accelerates and then decelerates as it diverts into the branches. The associated WSS is low at the impingement region and high further downstream, with, along the branch, first high positive and then high negative gradients (Dolan et al, 2013). By complementing animal studies with CFD simulations, Meng and colleagues have gathered evidence indicating that the combination of high WSS and positive WSSG triggers the pathological remodeling leading to aneurysm formation (Meng et al, 2007; Metaxa et al, 2010; Dolan et al, 2013). Other CFD studies, using pre-aneurysm images, have corroborated this finding (Kulcsar et al, 2011;

Kono and Terada, 2013; Kono et al, 2014). With respect to the rest of the branch and the controls, we also found aneurysms to form in regions of relatively high WSS and WSSG. However, although regions of positive WSSG were found close to the bifurcation apex, aneurysms were located further downstream in regions of mixed positive and negative WSSG.

Aneurysms also occur at locations with lesser-known hemodynamic conditions. Studying these locations can provide great insight into the hemodynamic mechanisms underlying aneurysm initiation. For instance, finding high WSS and WSSG in regions that are not commonly dominated by those WSS characteristics, which can be confirmed with controls, would provide stronger evidence in support of their role in aneurysm initiation. Recently, Lauric et al. reported on a study of 10 aneurysms located at the inner wall of the carotid siphon and 25 control ICAs (Lauric et al, 2014). The location was of particular interest as little was known about the hemodynamic conditions, except that the WSS was expected to be low. They found that aneurysms had formed in regions of low WSS flanked by peaks of high WSS and WSSG; WSS peaks correlated with the aneurysm necks; and controls were characterized by low, almost constant, WSS and WSSG. Similarly, in our study, comparing ACAs harboring aneurysms to ACAs that never formed an aneurysm allowed us to differentiate between hemodynamic stress patterns common to ACAs and those specific to aneurysm formation.

4.3 Temporal variation in WSS direction

Apart from their magnitudes, research has also focused on the oscillatory nature of the WSS and WSSG vectors. The most commonly used variable in this regard is the oscillatory shear index (OSI), which was introduced in the context of atherosclerosis (Ku et al, 1985) but later also used to study aneurysm initiation (Shimogonya et al, 2009; Singh et al, 2010; Kono et al, 2014) and rupture (Xiang et al, 2011; Miura et al, 2013). Two other variables were introduced specifically to study aneurysm initiation: the (potential) aneurysm formation indicator (AFI) (Mantha et al, 2006) and the gradient oscillatory number (GON) (Shimogonya et al, 2009). Variable definitions and results for these variables are presented in the appendix (Section 6)

Peiffer et al. recently proposed the transWSS and showed that it captures different flow features than OSI (Peiffer et al, 2013a). Preliminary results indicated strong correlations with atherosclerotic lesion. Other than OSI and AFI, which give more weight to flow reversal, transWSS focuses solely on the multidirectional (vs. uniaxial) nature of disturbed flow. Given these unique properties, we considered it a relevant new variable to assess in the context of aneurysm initiation.

For both cases and controls, regions of high transWSS were concentrated, suggesting that flow disturbances remained in the same location throughout the cardiac cycle. As expected, flow was more disturbed closer to the ICA bifurcation, leading to higher transWSS values in that region. Averaged over the whole, cases were found to have significantly higher transWSS values, but there were no clear correlations with the aneurysm initiation site.

4.4 Temporal variation in WSS magnitude

Among the assessed hemodynamic variables, WSSPI most consistently coincided with the aneurysm initiation site. The variable was introduced as a simple metric to quantify the temporal variation of the WSS magnitude without using noise-prone temporal gradients (Lee et al, 2009). Besides the spatial variation in the WSS magnitude, related to the WSSG, and the temporal variation in the WSS direction, our results suggest that the temporal variation in the WSS magnitude is also an important factor to consider when investigating the role of hemodynamic stress in aneurysm initiation. This is in line with the observation that endothelial cells respond differently to temporal vs. spatial variations in WSS (White et al, 2001, 2005) and to different types of pulsatile flow (Helmlinger et al, 1991; Himburg et al, 2007; Feaver et al, 2013).

4.5 Limitations and future directions

Aneurysms were virtually removed to approximate the pre-aneurysm vascular geometry. This approach has two main limitations. First, manual removal of aneurysms is observer-dependent. We addressed this by repeating the analysis with a second observer and found good agreement (Figure 8). Other studies employed automatic removal methods (Ford et al, 2009; Shimogonya et al, 2009; Chen et al, 2013), but these preserve less of the vascular geometry and still rely on manually set parameters. Second, aneurysm removal does not account for possible changes in parent vessel geometry due to interaction with the perianeurysmal environment during aneurysm growth (Sforza et al, 2012). Since ICA bifurcations are not near bone structures, substantial changes were unlikely to have occurred. However, prospective studies are needed for confirmation.

Discrepancies between estimated and patient-specific flow rate waveforms at the inlet have been shown to strongly affect the WSS magnitude (Karmonik et al, 2010; Marzo et al, 2011; Jansen et al, 2014; McGah et al, 2014), but not the WSS distribution (Marzo et al, 2011). Therefore, we focused on the distribution by normalizing appropriate variables by the average WSS on the branch. We also repeated the analysis with a 20 % higher inflow rate to confirm that the WSS distribution remained relatively unchanged. The influence of the waveform shape on the WSSPI should be investigated. Regarding the outlets, despite the simplification of zero-pressure boundary conditions, the resulting ACA:MCA flow split of 34:66 closely matched the in vivo measurements (36:64) reported in (Zhao et al, 2007). Although much can be learned from WSS distributions, we wish to stress that CFD studies scrutinizing the role of hemodynamics in aneurysm initiation and rupture would greatly benefit from patient-specific boundary conditions. Ideally, a range of possible boundary conditions, covering all the patient's levels of exercise, should be considered to obtain a complete picture of the shear stresses exerted on the arterial wall.

Pathogenesis of cerebral aneurysms involves the interplay between mechanical stimuli, vascular biology, and vascular geometry (Meng et al, 2014). Therefore, aneurysm initiation is likely caused by a combination of biochemical and biomechanical fac-

tors (Sadasivan et al, 2013). Although hemodynamic stresses appear to be important, their effect on the vascular biology, i.e. the mechanobiology, should also be modeled to gain a deeper understanding of the underlying mechanisms (Humphrey and Taylor, 2008; Watton et al, 2009, 2010). Moreover, among hemodynamic stresses, not only the WSS but also pressure-induced tensile stresses are known regulators of vascular biology and should be analyzed (Meng et al, 2014).

5 Conclusions

The aim of this study was to analyze the WSS field at the aneurysm initiation site. Ten cases with aneurysms at a single location were analyzed and compared with ten controls. We found that the general region in which aneurysms had formed was characterized by high TAWSS and high TAWSSG. The aneurysm initiation site partly overlapped with regions of high TAWSS and, among all assessed variables, most consistently coincided with peaks of WSSPI.

6 Open data

To promote the future use of the dataset, surface meshes of all cases (with and without aneurysm) and controls have been made available online at (Geers et al, 2015b).

Conflict of interest

None.

Acknowledgements Financial support for this work was provided by the European Commission through the @neurIST project (FP6-IST-027703). The authors are very grateful to all collaborators within the @neurIST project. In particular, we would like thank the following institutes for directly contributing to the construction of the @neurIST database (in alphabetical order): Advanced Simulation & Design GmbH, Rostock, Germany (C. Bludszuweit-Philipp); ANSYS Europe Ltd, Abingdon, UK (I. Jones, J. Penrose); BioComputing Competence Centre, Super Computing Solution s.r.l., Bologna, Italy (A. Chiarini, M. Viceconti); Hospital Clínic i Provincial de Barcelona, Barcelona, Spain (J. Blasco, J. Macho); Hospital General de Catalunya, Sant Cugat del Vallès, Spain (T. Sola, E. Vivas); Hôpitaux Universitaires de Genève, Geneva, Switzerland (P. Bijlenga, M. Jägersberg, K.O. Lovblad, A. Marcos-Gonzalez, V. Mendes-Pereira, A.P. Narata, A. Rogers, D.A. Rüfenacht, K. Schaller, B. Schatlo, P. Teta); Royal Hallamshire Hospital, Sheffield, UK (S. Coley, P. Lawford, U. Patel, P. Singh, A. Waterworth); Universitat Pompeu Fabra, Barcelona, Spain (M.L. Aguilar, H. Bogunovic, G. Engelbrecht, A.F. Frangi, A.J. Geers, M. Kim, I. Larrabide, H.G. Morales, C. Valencia-Muñoz, M.C. Villa-Uriol); University of Sheffield, Sheffield, UK (D.R. Hose, R. Lycett, A. Marzo).

Appendix: Additional hemodynamic variables

This appendix presents variable definitions and results for three additional hemodynamic variables describing the oscillatory nature of the WSS and WSSG vectors.

The oscillatory shear index (OSI) was introduced by Ku et al. (Ku et al, 1985) and later redefined by He and Ku (He and Ku, 1996). It describes the oscillatory nature of the WSS vector, τ_w, during the cardiac cycle and has been used extensively in the context of atherosclerosis (Peiffer et al, 2013b) and aneurysm initiation (Singh et al, 2010; Shimogonya et al, 2009; Kono et al, 2014). It is given by

$$\mathrm{OSI} = \frac{1}{2}\left(1 - \frac{\left|\int_0^T \tau_w \,\mathrm{d}t\right|}{\int_0^T |\tau_w| \,\mathrm{d}t}\right), \qquad \mathrm{OSI} \in [0, \frac{1}{2}] \tag{8}$$

where t is time and T is the cardiac period.

The (potential) aneurysm formation indicator (AFI) was proposed by Mantha et al. (Mantha et al, 2006) to identify flow stagnation zones, which in their study of three sidewall aneurysms coincided with the aneurysm initiation site. It measures the cosine of angle θ between the instantaneous WSS vector and the time-averaged WSS vector, that is,

$$\mathrm{AFI} = \cos\theta = \frac{\tau_w}{|\tau_w|} \cdot \hat{p}, \qquad \mathrm{AFI} \in [-1, 1] \tag{9}$$

AFI was obtained at time point H1 of Ford et al.'s flow rate waveform (Ford et al, 2005), corresponding to midsystolic deceleration during which flow is least stable (Fung, 1997, p. 137).

The gradient oscillatory number (GON) was proposed by Shimogonya et al. (Shimogonya et al, 2009) to quantify the degree of oscillating tension/compression forces at the aneurysm initiation site. It is given by

$$\mathrm{GON} = 1 - \frac{\left|\int_0^T G \,\mathrm{d}t\right|}{\int_0^T |G| \,\mathrm{d}t}, \qquad \mathrm{GON} \in [0, 1] \tag{10}$$

where

$$G = \begin{pmatrix} \nabla_S (\tau_w \cdot \hat{p}) \cdot \hat{p} \\ \nabla_S (\tau_w \cdot \hat{q}) \cdot \hat{q} \end{pmatrix} \tag{11}$$

Contour plots of the three variables are in Figures 9 (OSI), 10 (AFI), and 11 (GON).

We found strong correlations between variables, implying that they capture the same flow features: AFI correlated with OSI, GON correlated with absolute TAWSSG. This is in accordance with previous studies (Lee et al, 2009; Peiffer et al, 2013a). The distribution of GON was very noisy, which can largely be attributed to it being the temporal variation in the second-order derivative of the velocity (Chen et al, 2013). No clear correlations were found between the variable distributions and the aneurysm initiation site.

References

Alfano JM, Kolega J, Natarajan SK, Xiang J, Paluch RA, Levy EI, Siddiqui AH, Meng H (2013) Intracranial aneurysms occur more frequently at bifurcation sites that typically experience higher hemodynamic stresses. Neurosurgery 73(3):497–505

Alnaes MS, Isaksen J, Mardal KA, Morgan BRMK, Ingebrigtsen T (2007) Computation of hemodynamics in the circle of Willis. Stroke 38(9):2500–2505

Antiga L, Steinman DA (2004) Robust and objective decomposition and mapping of bifurcating vessels. IEEE Transactions on Medical Imaging 23(6):704–713

Antiga L, Piccinelli M, Botti LA, Ene-Iordache B, Remuzzi A, Steinman DA (2008) An image-based modeling framework for patient-specific computational hemodynamics. Medical and Biological Engineering and Computing 46(11):1097–1112

Baek H, Jayaraman MV, Karniadakis GE (2009) Wall shear stress and pressure distribution on aneurysms and infundibulae in the posterior communicating artery bifurcation. Annals of Biomedical Engineering 37(12):2469–2487

Baharoglu MI, Lauric A, Wu C, Hippelheuser JE, Malek AM (2014) Deviation from optimal vascular caliber control at middle cerebral artery bifurcations harboring aneurysms. Journal of Biomechanics 47(13):3318–3324

Bogunović H, Pozo JM, Villa-Uriol MC, Majoie CB, van den Berg R, Gratama van Andel HAF, Macho JM, Blasco J, San Román L, Frangi AF (2011) Automated segmentation of cerebral vasculature with aneurysms in 3DRA and TOF-MRA using geodesic active regions: An evaluation study. Medical Physics 38(1):210–222

Brown RD, Wiebers DO, Forbes GS (1990) Unruptured intracranial aneurysms and arteriovenous malformations: Frequency of intracranial hemorrhage and relationship of lesions. Journal of Neurosurgery 73(6):859–863

Castro MA, Putman CM, Cebral JR (2011) Computational analysis of anterior communicating artery aneurysm shear stress before and after aneurysm formation. Journal of Physics: Conference Series 332:012,001

Cebral JR, Castro M, Putman CM, Alperin N (2008) Flow-area relationship in internal carotid and vertebral arteries. Physiological Measurement 29(5):585–594

Chen H, Selimovic A, Thompson H, Chiarini A, Penrose J, Ventikos Y, Watton PN (2013) Investigating the influence of haemodynamic stimuli on intracranial aneurysm inception. Annals of Biomedical Engineering 41(7):1492–1504

Doenitz C, Schebesch KM, Zoephel R, Brawanski A (2010) A mechanism for the rapid development of intracranial aneurysms: a case study. Neurosurgery 67(5):1213–1221

Dolan JM, Kolega J, Meng H (2013) High wall shear stress and spatial gradients in vascular pathology: A review. Annals of Biomedical Engineering 41(7):1411–1427

Feaver RE, Gelfand BD, Blackman BR (2013) Human haemodynamic frequency harmonics regulate the inflammatory phenotype of vascular endothelial cells. Nature Communications 4:1525

Ford MD, Alperin N, Lee SH, Holdsworth DW, Steinman DA (2005) Characterization of volumetric flow rate waveforms in the normal internal carotid and vertebral

arteries. Physiological Measurement 26(4):477–488
Ford MD, Hoi Y, Piccinelli M, Antiga L, Steinman DA (2009) An objective approach to digital removal of saccular aneurysms: Technique and applications. The British Journal of Radiology 82(SI-1):S55–S61
Foutrakis GN, Yonas H, Sclabassi RJ (1999) Saccular aneurysm formation in curved and bifurcating arteries. American Journal of Neuroradiology 20(7):1309–1317
Frösen J (2014) Smooth muscle cells and the formation, degeneration, and rupture of saccular intracranial aneurysm wall: A review of current pathophysiological knowledge. Translational Stroke Research 5(3):347–356
Fung YC (1997) Biomechanics: Circulation, 2nd edn. Springer
Geers AJ, Larrabide I, Radaelli AG, Bogunović H, Kim M, Gratama van Andel HAF, Majoie CB, VanBavel E, Frangi AF (2011) Patient-specific computational hemodynamics of intracranial aneurysms from 3D rotational angiography and CT angiography: An in vivo reproducibility study. American Journal of Neuroradiology 32(3):581–586
Geers AJ, Larrabide I, Morales HG, Frangi AF (2014) Approximating hemodynamics of cerebral aneurysms with steady flow simulations. Journal of Biomechanics 47(1):178–185
Geers AJ, Morales HG, Larrabide I, Butakoff C, Bijlenga P, Frangi AF (2015a) Wall shear stress at the initiation site of cerebral aneurysms: Distribution on flattened branches. Figshare URL http://dx.doi.org/10.6084/m9.figshare.1153934
Geers AJ, Morales HG, Larrabide I, Butakoff C, Villa-Uriol MC, Engelbrecht G, Bijlenga P, Frangi AF (2015b) Wall shear stress at the initiation site of cerebral aneurysms: Vascular models. Figshare URL http://dx.doi.org/10.6084/m9.figshare.1159108
Gonzalez CF, Cho YI, Ortega HV, Moret J (1992) Intracranial aneurysms: Flow analysis of their origin and progression. American Journal of Neuroradiology 13(1):181–188
Gosling RG, King DH (1974) Arterial assessment by Doppler-shift ultrasound. Proceedings of the Royal Society of Medicine 67(6 Pt 1):447–449
He X, Ku DN (1996) Pulsatile flow in the human left coronary artery bifurcation: Average conditions. Journal of Biomechanical Engineering 118(1):74–82
Helmlinger G, Geiger RV, Schreck S, Nerem RM (1991) Effects of pulsatile flow on cultured vascular endothelial cell morphology. Journal of Biomechanical Engineering 113(2):123–131
Himburg HA, Dowd SE, Friedman MH (2007) Frequency-dependent response of the vascular endothelium to pulsatile shear stress. American Journal of Physiology: Heart and Circulatory Physiology 293(1):H645–H653
Hop JW, Rinkel GJ, Algra A, van Gijn J (1997) Case-fatality rates and functional outcome after subarachnoid hemorrhage: a systematic review. Stroke 28(3):660–664
Humphrey JD, Taylor CA (2008) Intracranial and abdominal aortic aneurysms: Similarities, differences, and need for a new class of computational models. Annual Review of Biomedical Engineering 10:221–246

Ingebrigtsen T, Morgan MK, Faulder K, Ingebrigtsen L, Sparr T, Schirmer H (2004) Bifurcation geometry and the presence of cerebral artery aneurysms. Journal of Neurosurgery 101(1):108–113

Jamous MA, Nagahiro S, Kitazato KT, Satoh K, Satomi J (2005) Vascular corrosion casts mirroring early morphological changes that lead to the formation of saccular cerebral aneurysm: An experimental study in rats. Journal of Neurosurgery 102(3):532–535

Jansen IGH, Schneiders JJ, Potters WV, van Ooij P, van den Berg R, VanBavel E, Marquering HA, Majoie CBLM (2014) Generalized versus patient-specific inflow boundary conditions in computational fluid dynamics simulations of cerebral aneurysmal hemodynamics. American journal of Neuroradiology 35(8):1543–1548

Karmonik C, Yen C, Diaz O, Klucznik R, Grossman RG, Benndorf G (2010) Temporal variations of wall shear stress parameters in intracranial aneurysms-importance of patient-specific inflow waveforms for CFD calculations. Acta Neurochirurgica 152(8):1391–1398

Kayembe KN, Sasahara M, Hazama F (1984) Cerebral aneurysms and variations in the Circle of Willis. Stroke 15(5):846–850

Kondo S, Hashimoto N, Kikuchi H, Hazama F, Nagata I, Kataoka H (1997) Cerebral aneurysms arising at nonbranching sites: An experimental Study. Stroke 28(2):398–403

Kono K, Terada T (2013) Hemodynamics of 8 different configurations of stenting for bifurcation aneurysms. American Journal of Neuroradiology 34(10):1980–1986

Kono K, Fujimoto T, Terada T (2014) Proximal stenosis may induce initiation of cerebral aneurysms by increasing wall shear stress and wall shear stress gradient. International Journal for Numerical Methods in Biomedical Engineering [Epub ahead of print]

Ku DN, Giddens DP, Zarins CK, Glagov S (1985) Pulsatile flow and atherosclerosis in the human carotid bifurcation: Positive correlation between plaque location and low oscillating shear stress. Arteriosclerosis 5(3):293–302

Kulcsar Z, Ugron A, Marosfoi M, Berentei Z, Paál G, Szikora I (2011) Hemodynamics of cerebral aneurysm initiation: The role of wall shear stress and spatial wall shear stress gradient. American Journal of Neuroradiology 32(3):587–594

Lauric A, Hippelheuser J, Safain MG, Malek AM (2014) Curvature effect on hemodynamic Conditions at the inner bend of the carotid siphon and its relation to aneurysm formation. Journal of Biomechanics [Epub ahead of print]

Lee SW, Antiga L, Steinman DA (2009) Correlations among indicators of disturbed flow at the normal carotid bifurcation. Journal of Biomechanical Engineering 131(6):061,013

Mantha AR, Karmonik C, Benndorf G, Strother C, Metcalfe RW (2006) Hemodynamics in a cerebral artery before and after the formation of an aneurysm. American Journal of Neuroradiology 27(5):1113–1118

Markl M, Frydrychowicz A, Kozerke S, Hope M, Wieben O (2012) 4D flow MRI. Journal of Magnetic Resonance Imaging 36(5):1015–1036

Marzo A, Singh PK, Larrabide I, Radaelli AG, Coley SC, Gwilliam M, Wilkinson I, Lawford PV, Reymond P, Patel U, Frangi AF, Hose DR (2011) Computational

hemodynamics in cerebral aneurysms: The effects of modeled versus measured boundary conditions. Annals of Biomedical Engineering 39(2):884–896

McGah P, Levitt MR, Barbour MC, Morton RP, Nerva JD, Mourad PD, Ghodke BV, Hallam DK, Sekhar LN, Kim LJ, Aliseda A (2014) Accuracy of computational cerebral aneurysm hemodynamics using patient-specific endovascular measurements. Annals of Biomedical Engineering 42(3):503–514

Meng H, Wang Z, Gao BL, Hoi Y, Metaxa EM, Swartz DD, Kolega J (2007) Complex hemodynamics at the apex of an arterial bifurcation induces vascular remodeling resembling cerebral aneurysm initiation. Stroke 38(6):1924–1931

Meng H, Tutino VM, Xiang JP, Siddiqui A (2014) High WSS or low WSS? Complex interactions of hemodynamics with intracranial aneurysm initiation, growth, and rupture: Toward a unifying hypothesis. American Journal of Neuroradiology 35(7):1254–1262

Metaxa EM, Tremmel M, Natarajan SK, Xiang JP, Paluch RA, Mandelbaum M, Siddiqui AH, Kolega J, Mocco J, Meng H (2010) Characterization of critical hemodynamics contributing to aneurysmal remodeling at the basilar terminus in a rabbit model. Stroke 41(8):1774–1782

Miura Y, Ishida F, Umeda Y, Tanemura H, Suzuki H, Matsushima S, Shimosaka S, Taki W (2013) Low wall shear stress is independently associated with the rupture status of middle cerebral artery aneurysms. Stroke 44(2):519–521

Morales HG, Larrabide I, Geers AJ, Roman LS, Blasco J, Macho JM, Frangi AF (2013) A virtual coiling technique for image-based aneurysm models by dynamic path planning. IEEE Transactions on Medical Imaging 32(1):119–129

Nealen A, Igarashi T, Sorkine O, Alexa M (2006) Laplacian mesh optimization. In: Proceedings of the 4th International Conference on Computer Graphics and Interactive Techniques in Australasia and Southeast Asia (GRAPHITE), Kuala Lumpur, Malaysia, pp 381–389

Nixon AM, Gunel M, Sumpio BE (2010) The critical role of hemodynamics in the development of cerebral vascular disease. Journal of Neurosurgery 112(6):1240–1253

Peiffer V, , Sherwin SJ, Weinberg PD (2013a) Computation in the rabbit aorta of a new metric – the transverse wall shear stress – to quantify the multidirectional character of disturbed blood flow. Journal of Biomechanics 46(15):2651–2658

Peiffer V, Sherwin SJ, Weinberg PD (2013b) Does low and oscillatory wall shear stress correlate spatially with early atherosclerosis? A systematic review. Cardiovascular Research 99(2):242–250

Penn DL, Komotar RJ, Connolly ES (2011) Hemodynamic mechanisms underlying cerebral aneurysm pathogenesis. Journal of Clinical Neuroscience 18(11):1435–1438

Piccinelli M, Veneziani A, D A Steinman DA, Remuzzi A, Antiga L (2009) A framework for geometric analysis of vascular structures: Application to cerebral aneurysms. IEEE Transactions on Medical Imaging 28(8):1141–1155

Piccinelli M, Bacigaluppi S, Boccardi E, Ene-Iordache B, Remuzzi A, Veneziani A, Antiga L (2011) Geometry of the internal carotid artery and recurrent patterns in location, orientation and rupture status of lateral aneurysms: An image-based computational study. Neurosurgery 68(5):1270–1285

Sadasivan C, Fiorella DJ, Woo HH, Lieber BB (2013) Physical factors effecting cerebral aneurysm pathophysiology. Annals of Biomedical Engineering 41(7):1347–1365

Sforza DM, Tateshima CMPS, nuela FV, Cebral JR (2012) Effects of perianeurysmal environment during the growth of cerebral aneurysms: A case study. American Journal of Neuroradiology 33(6):1115–1120

Shimogonya Y, Ishikawa T, Imai Y, Matsuki N, Yamaguchi T (2009) Can temporal fluctuation in spatial wall shear stress gradient initiate a cerebral aneurysm? A proposed novel hemodynamic index, the gradient oscillatory number (GON). Journal of Biomechanics 42(4):550–554

Singh PK, Marzo A, Howard B, Rüfenacht DA, Bijlenga P, Frangi AF, Lawford PV, Coley SC, Hose DR, Patel UJ (2010) Effects of smoking and hypertension on wall shear stress and oscillatory shear index at the site of intracranial aneurysm formation. Clinical Neurology and Neurosurgery 112(4):306–313

Stehbens WE (1989) Etiology of intracranial berry aneurysms. Journal of Neurosurgery 70(6):823–831

Tremmel M, Xiang JP, Hoi Y, Kolega J, Siddiqui A, Mocco J, Meng H (2010) Mapping vascular response to in vivo Hemodynamics: Application to increased flow at the basilar terminus. Biomechanics and Modeling in Mechanobiology 9(4):421–434

Turjman AS, Turjman F, Edelman ER (2014) Role of fluid dynamics and inflammation in intracranial aneurysm formation. Circulation 129(3):373–382

Villa-Uriol MC, Berti G, Hose DR, Marzo A, Chiarini A, Penrose J, Pozo JM, Schmidt JG, Singh PK, Lycett R, Larrabide I, Frangi AF (2011) @neurIST complex information processing toolchain for the integrated management of cerebral aneurysms. Interface Focus 1(3):308–319

Watton PN, Raberger NB, Holzapfel GA, Ventikos Y (2009) Coupling the hemodynamic environment to the evolution of cerebral aneurysms: Computational framework and numerical examples. Journal of Biomechanical Engineering 131(10):101,003

Watton PN, Selimovic A, Raberger NB, Huang P, Holzapfel GA, Ventikos Y (2010) Modelling evolution and the evolving mechanical environment of saccular cerebral aneurysms. Biomechanics and Modeling in Mechanobiology 10(1):109–132

White CR, Haidekker M, Bao X, Frangos JA (2001) Temporal gradients in shear, but not spatial gradients, stimulate endothelial cell proliferation. Circulation 103(20):2508–2513

White CR, Stevens HY, Haidekker M, Frangos JA (2005) Temporal gradients in shear, but not spatial gradients, stimulate ERK1/2 activation in human endothelial cells. American Journal of Physiology: Heart and Circulatory Physiology 289(6):H2350–H2355

Xiang JP, Natarajan SK, Tremmel M, Ma D, Mocco J, Hopkins LN, Siddiqui AH, Levy EI, Meng H (2011) Hemodynamic-morphologic discriminants for intracranial aneurysm rupture. Stroke 42(1):144–152

Zhao M, Amin-Hanjani S, Ruland S, Curcio AP, Ostergren L, Charbel FT (2007) Regional cerebral blood flow using quantitative MR angiography. American Journal of Neuroradiology 28(8):1470–1473

Fig. 1 Vascular models of cases with aneurysm (top), cases with the aneurysm virtually removed (middle), and controls (bottom). The ACA is colored red. View points were selected to best visualize the vascular model, so images are not necessarily at the same scale.

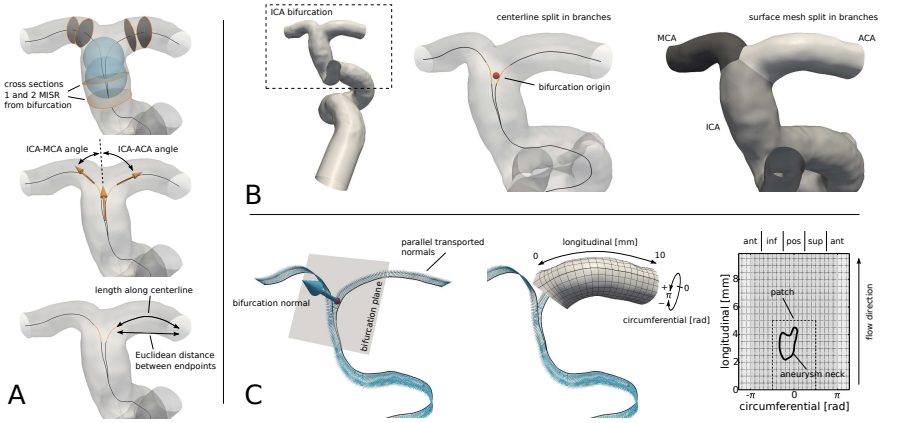

Fig. 2 Post-processing steps. A. Bifurcation sections were created one and two maximally inscribed sphere radii (MISR) away from the bifurcation to obtain representative cross sectional areas for the ICA, ACA and MCA. Bifurcation vectors projected onto the bifurcation plane (panel C) were used to calculate the bifurcation angles. The tortuosity was defined by Eq. (7) using the branch length along the centerline and the Euclidean distance between its endpoints. B. Centerlines from inlet to ACA outlet and inlet to MCA outlet diverged at the ICA bifurcation and were split into branches. Correspondingly, the vessel wall surface was also split into branches. C. The posteriorly directed normal to the bifurcation plane was parallel transported along the centerline. The ACA was mapped onto a 2D parametric space with a longitudinal and a circumferential coordinate. To view the distribution of hemodynamic variables on the whole branch at once, it was flattened onto a rectangle. Plots of the flattened branch indicate the location of the aneurysm neck and the patch. They also indicate the location of the posterior (pos), anterior (ant), superior (sup) and inferior (inf) sides of the branch. The plot range of the circumferential coordinate was slightly extended to show the continuity of the variable distribution. Duplicated regions were grayed out.

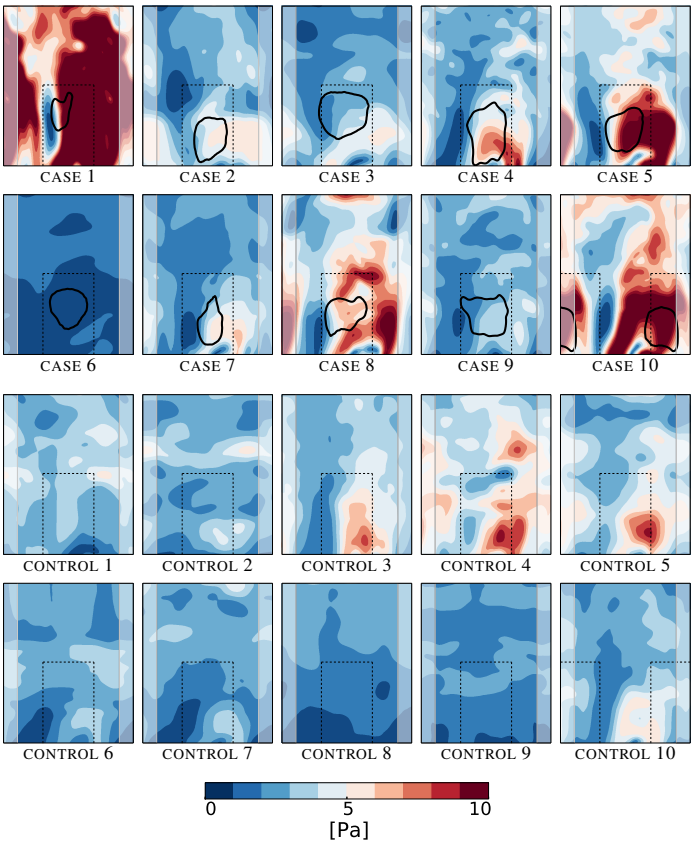

Fig. 3 Time-averaged WSS (TAWSS) under 'normal' inflow conditions. The same colormap range was used for all cases and controls. Plot properties are explained in Figure 2C.

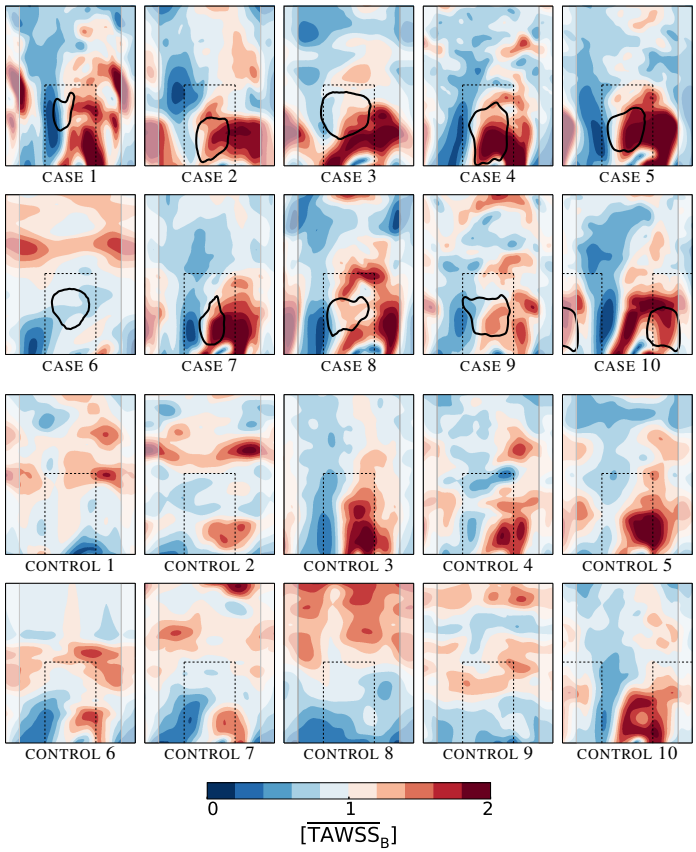

Fig. 4 Time-averaged WSS (TAWSS) under 'normal' inflow conditions. Colormaps were normalized by using $\overline{\text{TAWSS}}_B$ as unit. Plot properties are explained in Figure 2C.

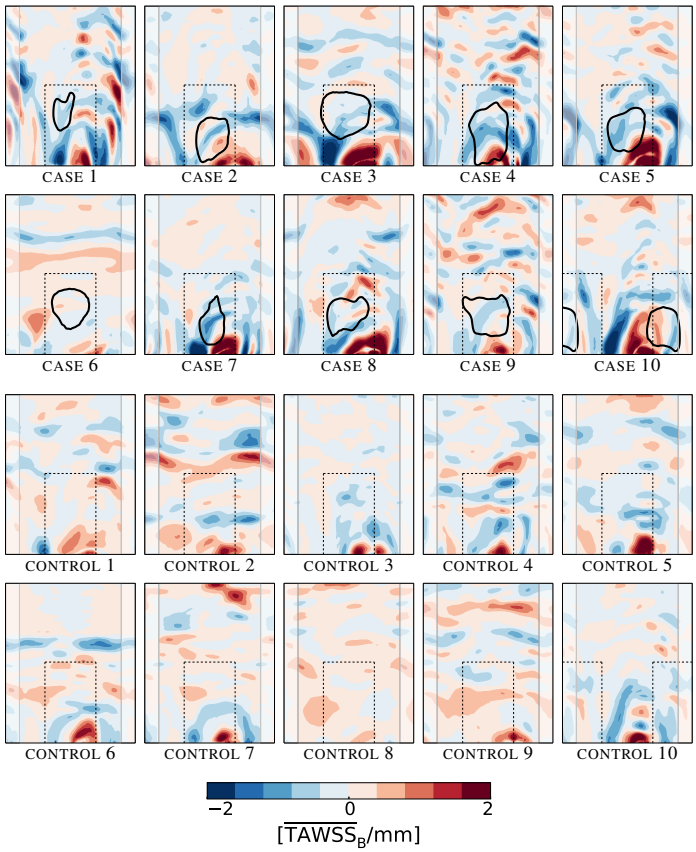

Fig. 5 Gradient of the time-averaged WSS (TAWSSG) under 'normal' inflow conditions. Colormaps were normalized by using $\overline{\text{TAWSS}}_B$/mm as unit. Plot properties are explained in Figure 2C.

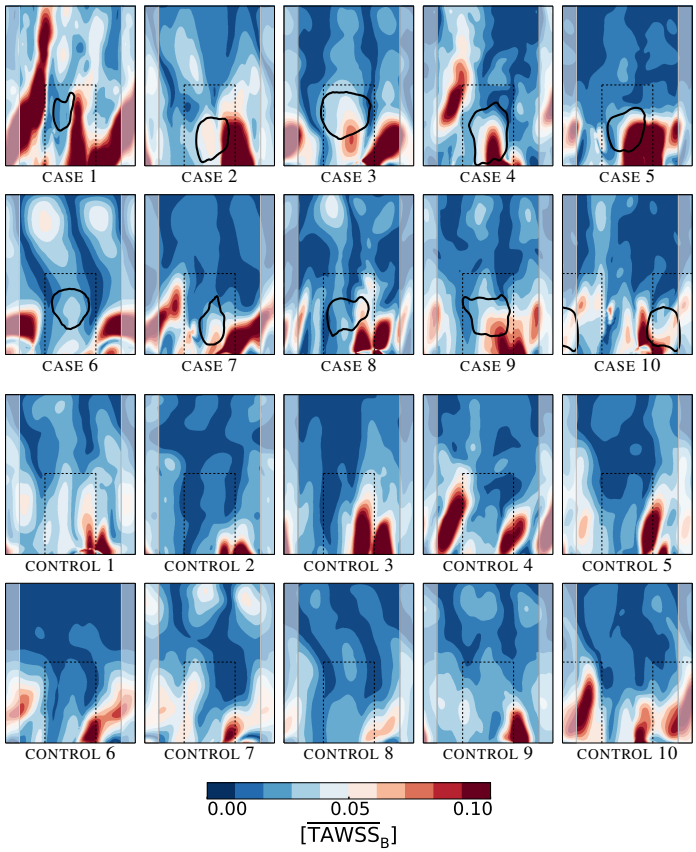

Fig. 6 Transverse WSS (transWSS) under 'normal' inflow conditions. Colormaps were normalized by using $\overline{\text{TAWSS}}_{\text{B}}$ as unit. Plot properties are explained in Figure 2C.

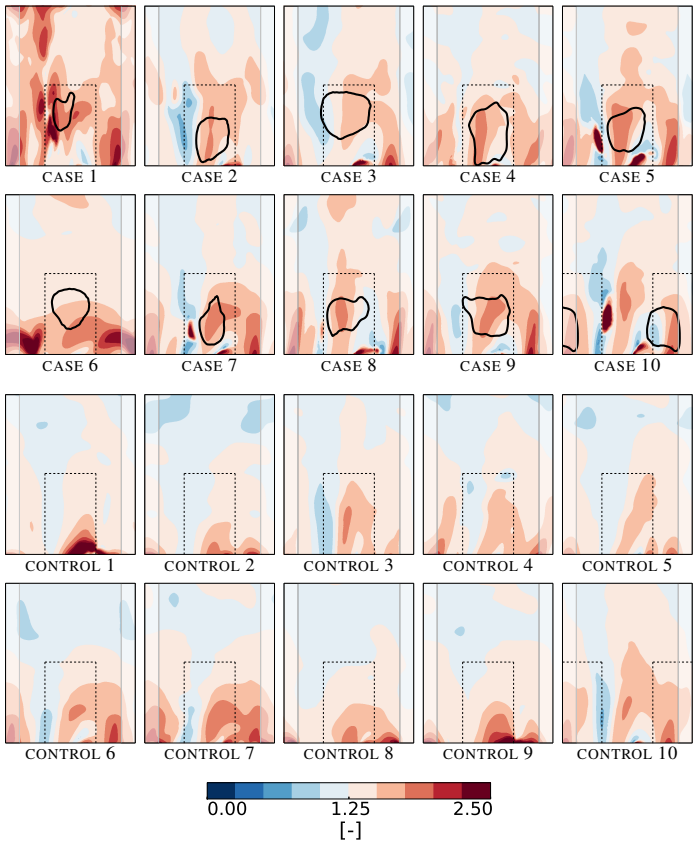

Fig. 7 WSS pulsatility index under 'normal' inflow conditions. The same colormap range was used for all cases and controls. Plot properties are explained in Figure 2C.

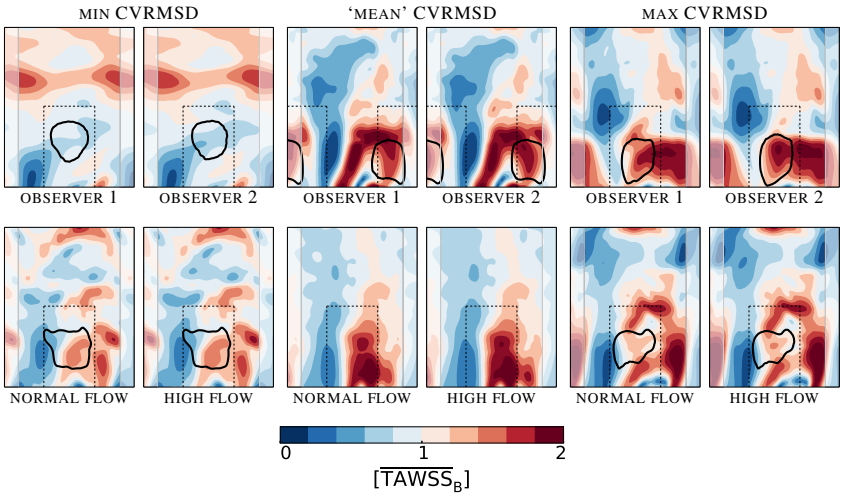

Fig. 8 Comparison of TAWSS distributions between observers removing the aneurysm and between 'normal' and 'high' flow rates at the inlet. Displayed are three cases or controls representating minimum, closest-to-mean and maximum CVRMSD. Colormaps were normalized by using $\overline{\text{TAWSS}}_\text{B}$ as unit. Plot properties are explained in Figure 2C.

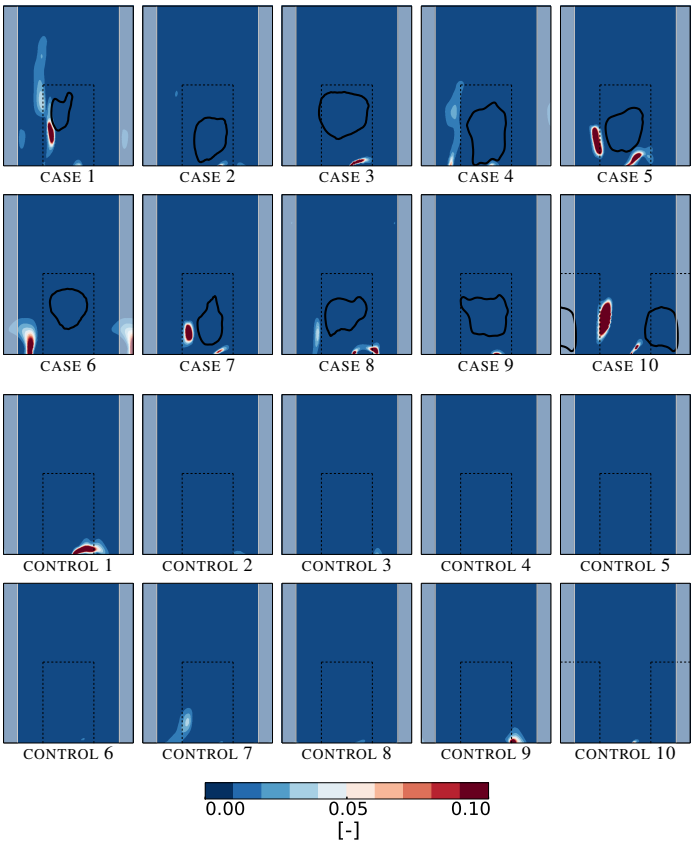

Fig. 9 Oscillatory shear index (OSI). Plot properties are explained in Figure 2C.

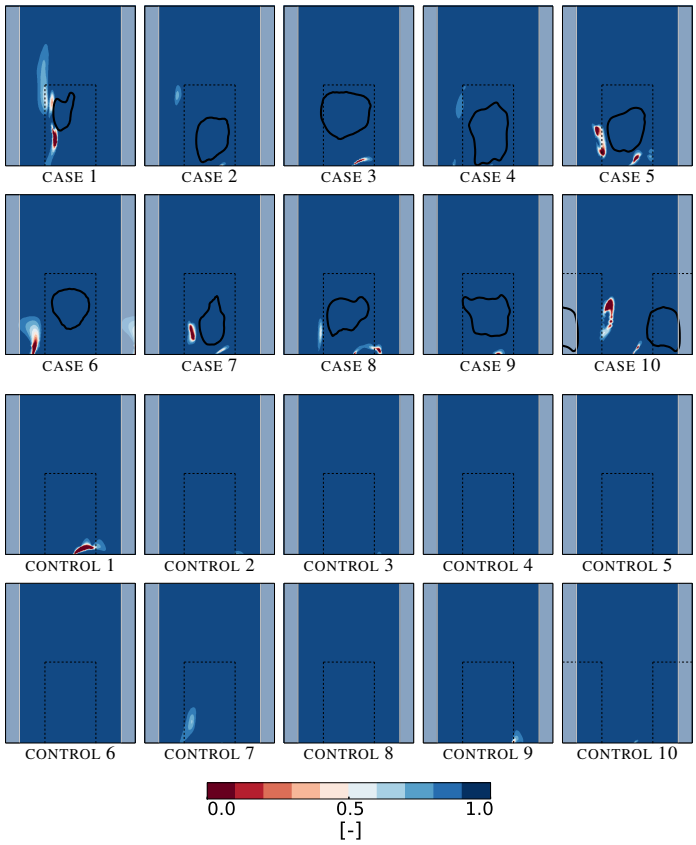

Fig. 10 Aneurysm formation indicator (AFI). Plot properties are explained in Figure 2C.

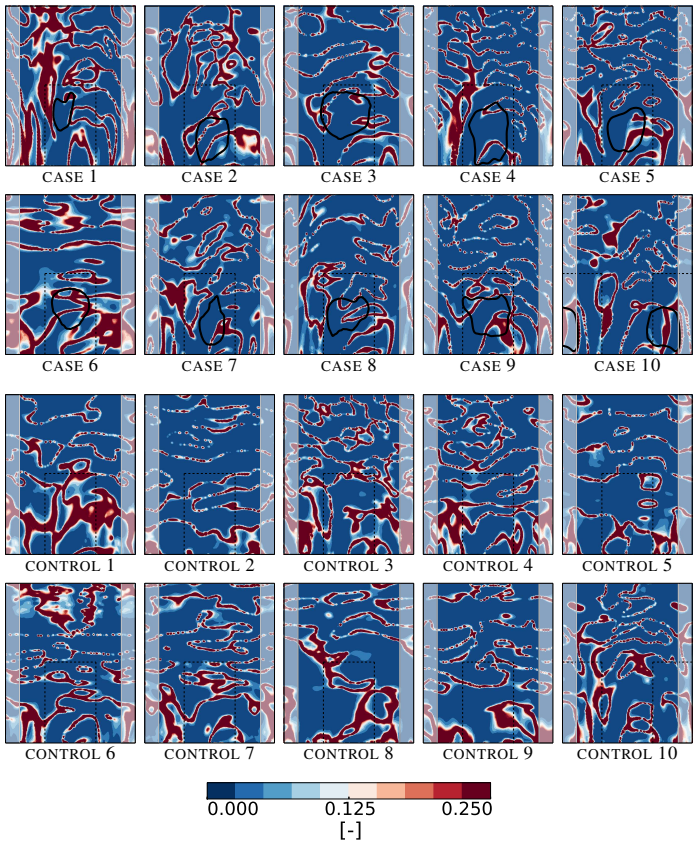

Fig. 11 Gradient oscillatory number (GON). Plot properties are explained in Figure 2C.

Table 1 Statistical analysis of geometric variables.

Variable	Unit	Mean and standard error		p-value[a]
		Cases	Controls	
ICA-ACA angle	[°]	77.8 ± 2.7	77.8 ± 3.1	.880
ICA-MCA angle	[°]	40.3 ± 2.5	39.4 ± 3.0	.940
ICA cross sectional area	[mm^2]	10.7 ± 0.8	9.5 ± 1.0	.364
ACA cross sectional area	[mm^2]	5.2 ± 0.6	3.8 ± 0.3	.059
MCA cross sectional area	[mm^2]	6.0 ± 0.3	5.1 ± 0.3	**.049**
ICA bifurcation area ratio	[-]	1.05 ± 0.05	0.98 ± 0.05	.545
ACA tortuosity	[-]	0.12 ± 0.03	0.06 ± 0.01	.059

[a] p-values were calculated with the Wilcoxon rank-sum test; values highlighted in bold face correspond to statistically significant differences with $p < 0.05$.

Table 2 Statistical analysis of hemodynamic variables.

		Mean and standard error of space-averaged variable values									
		Cases			Controls			p-value[b]			
Variable	Unit	Patch	Non-patch	Branch	Patch	Non-patch	Branch	I	II	III	IV
TAWSS	$[\overline{\mathrm{TAWSS}}_\mathrm{B}]$	1.18±0.05	0.94±0.02	1.00±0.00	1.01±0.05	1.00±0.02	1.00±0.00	**.022**	.959	**.034**	1.00
TAWSSG[a]	$[\overline{\mathrm{TAWSS}}_\mathrm{B}/\mathrm{mm}]$	0.53±0.05	0.34±0.02	0.39±0.02	0.35±0.03	0.26±0.02	0.28±0.02	**.017**	**.013**	**.010**	**.003**
transWSS	$[10^{-3}\,\overline{\mathrm{TAWSS}}_\mathrm{B}]$	42.7±3.9	26.1±3.0	30.4±2.7	31.4±3.2	21.4±1.1	23.7±1.3	**.007**	**.005**	.059	**.028**
WSSPI	[-]	1.52±0.03	1.38±0.03	1.41±0.03	1.45±0.02	1.27±0.02	1.32±0.02	**.005**	**.005**	.082	**.003**

[a] TAWSSG differentiates between positive and negative gradients, so we space-averaged the absolute TAWSSG.
[b] p-values were calculated with the Wilcoxon rank-sum test; the following samples were compared: I. patch vs. non-patch for the cases (paired), II. patch vs. non-patch for the controls (paired), III. patches of the cases vs. patches of the controls (unpaired), and IV. branches of the cases vs. branches of the controls (unpaired); values highlighted in bold face correspond to statistically significant differences with $p < 0.05$.